

1 ***Drosophila scribble* mutant tumors undergo a transition from a growth arrest state**
2 **to a proliferative state over time**

3

4 Tiantian Ji^{1,2*}, Lina Zhang^{1,2*}, Shengshuo Huang^{1,2,3}, Mingxi Deng^{1,2}, Ying Wang^{1,2,3},
5 Tri Thanh Pham⁴, Clemens Cabernard⁴, Jiguang Wang^{1,2,3}, Yan Yan^{1,2}

6

7 ¹Division of Life Science, Hong Kong University of Science and Technology, Clear
8 Water Bay, Kowloon, Hong Kong, China

9 ²Center of Systems Biology and Human Health, School of Science and Institute for
10 Advanced Study, Hong Kong University of Science and Technology, Clear Water Bay,
11 Kowloon, Hong Kong, China

12 ³Department of Chemical and Biological Engineering, Hong Kong University of Science
13 and Technology, Clear Water Bay, Kowloon, Hong Kong, China

14 ⁴Department of Biology, University of Washington, 24 Kincaid Hall, Seattle, WA 98105,
15 USA

16

17 *These authors contributed equally to this work

18

19 To whom correspondence should be addressed:

20 Yan Yan, Division of Life Science, Center of Systems Biology and Human Health, Hong
21 Kong University of Science and Technology, Clear Water Bay, Hong Kong, China. Tel:
22 (852)23585929; Email: yany@ust.hk

23

24

25

26 **Summary:**

27

28 The *Drosophila* neoplastic tumor suppressor gene (nTSG) mutant tumors have
29 successfully modeled many aspects of human tumor progression. However, the fly nTSG
30 mutant tumors progress rapidly over days. This is in contrast with most human tumors
31 which develop slowly, harbor heterogeneous cell populations for selection and undergo
32 an evolution-like process. Whether the fast-growing fly nTSG mutant tumors have
33 capacity for evolution remains unclear. Through quantitative analysis of the *scrib* mutant
34 tumor growth, we found that the *scrib* mutant tumors evolve to display different growth
35 rates and cell cycle profiles over time. Multiple growth-regulatory signaling pathways
36 show quantitative differences in early versus late *scrib* mutant tumors. These data suggest
37 that the *scrib* mutant tumors undergo a transition from a growth arrest state to a
38 proliferative state. Through longitudinal single cell RNA (scRNA) data analysis we found
39 that the *scrib* mutant tumors harbor heterogeneous cell populations likely of distinct
40 proliferative states, which are available for potential selection. This study raises the
41 possibility of studying tumor evolution in a genetically accessible and fast-growing
42 invertebrate tumor model.

43

44 **Introduction**

45

46 Proteins essential for maintaining epithelial structures, such as cell polarity complexes,
47 are involved in growth control (Bilder, 2004; Boggiano and Fehon, 2012; Sun and Irvine,
48 2016). For example, the basolateral Scribble complex, composed of Scribble (Scrib),
49 Discs large (Dlg) and Lethal giant larvae (L(2)gl), were discovered as a group of
50 “neoplastic tumor suppressor genes” (nTSGs) in *Drosophila* (Bilder et al., 2000; Bilder
51 and Perrimon, 2000; Gateff, 1978; Woods and Bryant, 1991). *Drosophila* larvae
52 homozygous mutant for any of the nTSGs grow into giant larvae with tumorous imaginal
53 discs and optic lobes. These mutant tumors fail to differentiate and grow into masses that
54 survive serial transplantations, induce cachexia and eventually kill the hosts (Figueroa-
55 Clarevega and Bilder, 2015; Gateff, 1978). Studies of *Drosophila* nTSGs over decades
56 have provided valuable insights into the mechanisms of growth control and tumorigenesis

57 (Bilder, 2004; Gonzalez, 2013; Pastor-Pareja and Xu, 2013; Richardson and Portela,
58 2018; Sonoshita and Cagan, 2017). For example, analyses of the nTSG mutant clonal
59 growth have revealed cell competition-mediated tumor suppression mechanisms, the
60 cooperative actions of multiple conserved signaling pathways during tumor development,
61 and tumor microenvironment influences (Brumby and Richardson, 2003; Chen et al.,
62 2012; Cordero et al., 2010; Igaki et al., 2006; Katheder et al., 2017; Pagliarini and Xu,
63 2003; Vaughn and Igaki, 2016; Yamamoto et al., 2017).

64

65 Interestingly, while the fly nTSG mutant tumors have successfully modeled many aspects
66 of human epithelial cancers, it was noted that for the fly nTSG tumors that progress
67 rapidly over days, a single gene mutation is sufficient to cause tumorigenesis. This is in
68 contrary to human tumors which typically develop slowly over months and years and
69 supported a multiple-hit model (Bilder, 2004; Hanahan and Weinberg, 2000; Nordling,
70 1953). Human tumors have been shown to display a variable degree of genetic and
71 epigenetic intratumor heterogeneity (ITH) that provides a foundation for selection and
72 tumor evolution (McGranahan and Swanton, 2017). Whether the fast-growing fly nTSG
73 mutant tumors have capacity for evolution has remained unclear.

74

75 Through quantitative analysis of the *scrib* mutant tumor growth, we found that over time
76 the *scrib* mutant tumors display different growth rates and cell cycle profiles. Moreover,
77 multiple signaling pathways display quantitative differences in early versus late *scrib*
78 mutant tumors. We demonstrated that high JNK signaling activity is a primary cause of
79 growth arrest in early *scrib* mutant tumors. These data suggest that the *scrib* mutant cells
80 undergo a transition from a growth arrest state to a proliferative state during tumor
81 progression. Longitudinal scRNA data analysis further reveals heterogeneity in the *scrib*
82 mutant tumors that potentially provides opportunities for selection and drives the
83 transition from a growth arrest state to a proliferative state as a population.

84

85 **Results**

86

87 **The *scrib* mutant tumors display different growth rates over time.**

88

89 To explore potential evolving traits during the *scrib* mutant tumor progression, we first
90 monitored the growth of wing imaginal discs derived from 3-hour egg collection of a
91 *scrib*¹/TM6B stock (Bilder and Perrimon, 2000) (Figure 1A-B). On average, at 4-day and
92 5-day after egg laying (AEL), the growth rate of the *scrib* mutant tumors is around 25%-
93 30% of that of control imaginal discs raised at identical conditions (Figure 1B). By 7-day
94 AEL the growth rate of the *scrib* mutant tumors is comparable with that of the 5-day AEL
95 control group (Figure 1B). Note that the *scrib* mutant tumors would continue growth to
96 sizes consistent with previous reports (Bilder et al., 2000; Gateff, 1978). Using phospho-
97 Histone H3 (PH3) as a marker for mitotic cells, we detected the 4-day AEL *scrib* mutant
98 tumors harbor much less PH3⁺ cells per unit volume than the control group (Figure 1C-D
99 and 1G). By 5-day AEL the *scrib* mutant tumors contain comparable number of PH3⁺
100 cells per unit volume with the control larvae as the wild type control group approached
101 the end of growth period (Figure 1E-F and 1G).

102

103 To test whether the initial slow-growth phenotype we observed in the early *scrib* mutant
104 tumors is specific to the *scrib*¹ allele, we generated tumors depleted of Scrib or Dlg at the
105 posterior region of wing discs through *engrailed*-Gal4 mediated RNAi. Although the
106 mosaic clones depleted of Scrib or Dlg are eliminated through cell competition (Brumby
107 and Richardson, 2003; Igaki et al., 2006; Vaughen and Igaki, 2016; Yamamoto et al.,
108 2017), the cell competition process does not cross segmentation boundary (Johnston,
109 2009; Morata and Ripoll, 1975; Simpson, 1979; Simpson and Morata, 1981). Therefore,
110 we can analyze the growth of the posterior *scrib* RNAi and *dlg* RNAi tumors independent
111 of the influence of cell competition. At 4-day and 5-day AEL, the volume of the *scrib*
112 RNAi and *dlg* RNAi tumors is much smaller than the size of the posterior region in
113 control wing discs (Figure 1H-Q). Meanwhile, the anterior regions of the *scrib* RNAi, *dlg*
114 RNAi and control imaginal discs have comparable average volumes (Figure 1H-Q),
115 indicating that the slow-growth phenotype observed in early *scrib* tumors is likely to be
116 independent of specific alleles used and an overall larval developmental delay.
117 Interestingly, from 4-day to 6-day AEL we could detect an increase of PH3⁺ cell number
118 in the posterior *scrib* RNAi and *dlg* RNAi tumors (Figure 1H-U), indicative of changes in

119 growth rates during tumor progression. Note that larvae harboring *scrib* RNAi or *dlg*
120 RNAi imaginal discs turned into pupae by 7-day AEL, preventing further measurement
121 of growth rates.

122

123 **The *scrib* mutant tumors show cell cycle defects that resolve over time.**

124

125 The small volume of early *scrib* mutant tumors can be caused through increased
126 apoptosis, defects in cellular growth or defective cell proliferation. We found that
127 prevention of apoptosis by overexpressing p35 could not rescue the growth arrest of the
128 posterior *scrib* RNAi cells (Figure S1A-H). Moreover, while we were able to detect
129 apoptotic cells in the posterior *scrib* RNAi region, a similar number of apoptotic cells can
130 also be detected in the anterior control region (Figure S1I). Therefore, the small volume
131 of early *scrib* mutant tumors is unlikely to be caused by increased apoptosis. The cell
132 volume of individual *scrib* mutant cells is larger than that of the control wing disc cells
133 (Figure S2A-B), consistent with a loss of epithelial packing and an elevation of mTOR
134 signaling activity in the *scrib* mutant cells (Figure S2C-F). Therefore, the growth arrest of
135 early *scrib* mutant tumors is also unlikely to be caused by defects in cellular growth.

136

137 Next, we examined additional proliferation markers in the *scrib* mutant tumors. Using 30-
138 min EdU incorporation as an indicator for S-phase cells, we noticed a significant decrease
139 in EdU incorporation in the 4-day AEL posterior *scrib* RNAi cells (Figure 2A, 2B and
140 2E). However, in 5-day AEL wing discs, we noticed that the posterior *scrib* RNAi cells
141 show similar EdU incorporation rate as the control group (Figure 2C, 2D and 2E). Flow
142 cytometry analysis showed a significant decrease of G1/S population in the posterior
143 *scrib* RNAi cells in comparison with the anterior control cells from 4-day AEL wing
144 discs (Figure 2F). By 5-day and 6-day AEL, the G1/S population in the posterior *scrib*
145 RNAi cells showed progressive recovery to a level comparable with that of the anterior
146 control cells (Figure 2G and 2H). We also observed a similar pattern of G1/S population
147 decrease from 4-day AEL *scrib* mutant tumors and recovery from 5-day *scrib* mutant
148 tumors in comparison with the control group (Figure 2I and 2J). Notably, flow cytometry
149 analysis detected a population of cells with higher DNA content than normal cells in the

150 4-day AEL *Scrib*-depleted cells (Figure 2F and 2I). Using the FUCCI system (Zielke et
151 al., 2014), we detected a population of G2/M cells (GFP+RFP+) with enlarged cell nuclei
152 in 4-day AEL *Scrib*-depleted cells (Supplemental Movie 1). Taken together, the above
153 data suggested that a population of 4-day AEL *scrib* mutant cells is arrested during G2/M
154 transition and a subset of these cells might re-initiate the DNA replication process before
155 entering mitosis.

156

157 *Drosophila* larval brain neuroblasts are an excellent model for analyzing mitosis due to
158 its accessibility for live imaging (Cabernard and Doe, 2013). We observed that the *scrib*
159 mutant neuroblasts displayed a significant prolonged entry into mitosis (Figure S3),
160 consistent with the cell cycle defects we observed in 4-day AEL *scrib* mutant wing disc
161 cells.

162

163 We conclude that the growth arrest of early *scrib* mutant tumors is most likely caused by
164 defects in cell cycle progression, yet the cell cycle defects observed in the early *scrib*
165 mutant tumors can resolve over time.

166

167 **The *scrib* mutant tumors display quantitative differences in multiple signaling**
168 **pathway activities over time.**

169

170 To investigate the reason why early and late *scrib* mutant tumors display different growth
171 rates and cell cycle profiles, we examined transcriptomes of *scrib* mutant tumors
172 collected at different time points. Principal component analysis (PCA) showed the
173 biological repeats of the *scrib* mutant tumors from the same stage are well-clustered and
174 the *scrib* mutant tumors form a transition trajectory along time (Figure 3A). Hierarchical
175 clustering further showed that the early and late *scrib* mutant tumors show distinctive
176 gene expression pattern (Figure 3B).

177

178 Interestingly, the time-course analysis showed that several signaling pathways previously
179 implicated in modulating the *scrib* mutant cell growth show quantitative changes in the
180 *scrib* mutant tumors over time. For example, the *unpaired (upd)* genes, the JAK/STAT

181 pathway ligands, are significantly regulated in the 8-day *scrib* mutant tumors in
182 comparison with the wild type control, with fold changes consistent with those reported
183 in a previous study (Figure S4A)(Bunker et al., 2015). Time-course analysis of the *upd*
184 family gene transcription reveals a peak expression in the 5-day AEL *scrib* mutant
185 tumors that decreases over time (Figure S4A). Meanwhile, the expression of *mirror*,
186 which is repressed by JAK/STAT transcriptional activity (Zeidler et al., 1999), shows
187 lowest expression level in 5-day AEL *scrib* mutant tumors that recovers over time
188 (Figure S4A). Notch, EGFR, JNK and Hippo signaling activities have been previously
189 shown to modulate the growth outcomes of the *scrib* mutant mosaic clones (Brumby and
190 Richardson, 2003; Chen et al., 2012; Igaki et al., 2006; Pagliarini and Xu, 2003). Similar
191 to the JAK/STAT pathway, a time-course analysis of well-established transcriptional
192 targets of Notch, EGFR and JNK signaling pathways reveals quantitative changes during
193 the *scrib* mutant tumor progression (Figure 3C-D, Figure S4). Therefore, it is likely that
194 quantitative changes in these signaling activities over time determine the differential
195 growth rates and cell cycle profiles we observed in early and late *scrib* mutant tumors.

196

197 In particular, the abnormally high JNK signaling activity or low Notch or low EGFR
198 signaling activity could be the underlying reason for the slow growth phenotype we
199 observed in early *scrib* mutant tumors. We found that the growth arrest phenotype in 4-
200 day and 5-day AEL posterior *scrib* tumors were rescued through overexpression of a
201 dominant-negative form of Basket (Bsk^{DN}) (Igaki et al., 2006)(Figure 3E-L) or a
202 dominant-negative form of Tak1 (Figure S5), which block JNK signaling activity.
203 Overexpression of Ras^{V12} and Notch intracellular domain (NICD) in combination with
204 *scrib* RNAi through *engrailed*-Gal4 caused lethality during embryogenesis or severe
205 overall developmental delay even with a temperature-sensitive form of tubulin-Gal80.
206 We therefore performed the growth analysis of *scrib* RNAi tumors in combination with
207 overexpression of Ras^{V12} using a C885a-Gal4 which expresses early to induce
208 tumorigenesis and does not cause overall developmental delay (Hrdlicka et al., 2002). We
209 found that overexpression of Ras^{V12} or NICD or Yki^{S168A} (an active form of Yki) cannot
210 rescue the slow growth phenotype in early *scrib* RNAi tumors (Figure 3M-S), even
211 though overexpression of Ras^{V12} and Yki^{S168A} showed growth-promoting effects in later

212 stages (Figure 3T). Note that overexpression of NICD with C885a-Gal4 still lead to
213 larvae of overall small body size and therefore small tumor size (Figure 3T). Taken
214 together, these data suggest that the slow growth phase in early *scrib* tumors is primarily
215 caused by high JNK signaling activity.

216

217 **The *scrib* mutant tumors harbor heterogeneous cell populations of different**
218 **proliferative states.**

219

220 The *scrib* mutant tumors display changes in growth rate and cell cycle profiles, as well as
221 quantitative differences in activities of multiple signaling pathways over time. These data
222 suggest that the *scrib* mutant tumors undergo a transition from a growth arrest state to a
223 proliferative state. To gain further insights into this transition, we built a
224 spatiotemporally-resolved transcriptomic landscape from staged *scrib* mutant tumors.

225

226 We profiled a minimum of 3000 cells per stage from 4-day, 5-day and 8-day AEL *scrib*
227 mutant tumors. We then pooled the *scrib* mutant cells from different stages together for
228 clustering and examined the distribution of four cell types defined by the expression
229 levels of the JNK signaling activity reporter *Mmp1* and the EGFR signaling reporter *kek1*.
230 *Mmp1^{high}* cell number decreases and *kek1^{high}* cell number increases over time, consistent
231 with the bulk RNA-seq data and validating the scRNA data quality (Figure 4A-B).
232 Moreover, *Mmp1* and *kek1* show significant biased distribution in single cells from
233 different stages (Figure S6), suggesting that the *scrib* mutant tumors might harbor
234 heterogeneous populations of cells at different proliferative states.

235

236 To further explore the distribution of potential cell states, we first used *Mmp1* and *kek1* as
237 marker genes to perform semi-supervised cell ordering in pseudotime with Monocle
238 (Trapnell et al., 2014) (Figure 4C-E). The expression of JNK and EGFR signaling
239 reporter genes show progressive changes along the pseudotime trajectory (Figure S7).
240 Interestingly, the Hippo signaling activity reporters *Diap1*, *expanded(ex)* and *Cyclin*
241 *E(CycE)* also show increase along the pseudotime trajectory (Figure S7), while these
242 genes do not show obvious changes over time (Figure S6). Similarly, genes that promote

243 cell cycle progression, such as *Cyclin B*, *Cdc25/string*, and *Cdc20/fizzy*, also show
244 increase along the pseudotime trajectory (Figure S7). Taken together, the pseudotime
245 trajectory likely reflects an arrest-to-proliferation state transition trajectory for the *scrib*
246 mutant cells. We found that single cells from tumors of different ages are scattered along
247 the pseudotime trajectory. Notably, the 4-day and 5-day AEL *scrib* mutant cells are more
248 enriched towards the arrested state of the pseudotime trajectory and the 8-day AEL *scrib*
249 mutant cells are enriched towards the opposite end along the trajectory (Figure 4E).

250

251 The above analysis is based on semi-supervised learning and the method assumes a tree-
252 like structure to distinguish cell states (Trapnell et al., 2014). To gain an unbiased view of
253 the *scrib* mutant cell states, we further adopted the scTDA, a nonlinear, model-
254 independent, and unsupervised topological data analysis (TDA) method for analyzing and
255 visualizing single-cell data (Rizvi et al., 2017). We randomly selected the same number
256 of cells from each stage and pooled these cells from all stages for analysis. Interestingly,
257 different random experiments robustly capture well-clustered cells that likely represent
258 the arrested state based on inspection of marker genes such as *Mmp1*, *kek1*, *CycE* and
259 *string* (Figure 4F and Figure S8). Moreover, cells from different ages are scattered on the
260 topological representation, again indicating that the *scrib* mutant tumors from all profiled
261 stages harbor heterogeneous cell populations. Notably, the cells at the arrest state are
262 more likely to be from the early stage tumors (Figure 4F and Figure S8). Interestingly,
263 while the arrest state is well-clustered and easily detectable, other cell states form
264 complex structures in the topological representations, indicating heterogeneous cell states
265 presented in the *scrib* mutant tumors are unlikely to be along a linear transition from the
266 least proliferative to the most proliferative state.

267

268 **Discussion**

269

270 Here we demonstrated that the *scrib* mutant tumors undergo a transition from a growth-
271 arrest state to a proliferation state over time and constructed a spatiotemporally resolved
272 evolution landscape for the *scrib* mutant tumors. Our data suggest that the *scrib* mutant

273 tumors harbor heterogeneous cell populations, providing a foundation for potential
274 selection and transition into a proliferation state as a population over time.
275
276 We do not yet know how cells of different proliferative states arise in undifferentiated
277 *scrib* mutant tumors. Notably, in flies a class of spindle assembly checkpoint mutations in
278 combination with apoptosis blockage can induce neoplastic tumor growth (Morais da
279 Silva et al., 2013). It is therefore interesting to speculate if the two types of neoplastic
280 tumor growth might partially share a common basis of generating heterogeneous cells
281 through genome instability. It is also possible that cells of different states arise from
282 stochasticity and the differences are amplified through complex feedback loops within
283 the cell-signaling network. It will be interesting to explore whether and how cell states
284 defined by combinatorial signaling activities are passed to daughter cells through
285 epigenetic markers. It will be also interesting to explore whether and how cells can transit
286 among different proliferative states.

287
288 The clonal *scrib* mutant cells are eliminated through cell competition when they are
289 surrounded by wild-type neighbors (Brumby and Richardson, 2003; Vaughn and Igaki,
290 2016; Yamamoto et al., 2017). It is noteworthy that the clonal *scrib* mutant cells are
291 likely to be in a different state from *scrib* mutant cells in early homozygous tumors.
292 Studies have shown overexpression of Ras^{V12}, NICD and p35 can effectively block the
293 clonal *scrib* mutant cells from apoptosis induced by cell competition (Brumby and
294 Richardson, 2003; Pagliarini and Xu, 2003). In our study, we found that overexpression
295 of Ras^{V12}, NICD and p35 have little effects in relieving the early *scrib* mutant tumors
296 from growth arrest. It will be interesting to profile the clonal *scrib* mutant cells in the
297 future and compare how the clonal *scrib* mutant cells change cell state in response to cell
298 competition signals.

299

300 **Experimental Procedures**

301

302 **Fly stocks**

303

304 The fly strains used in this study were: *scrib*¹ FRT82B/TM6B (Bilder et al., 2000), UAS-
305 *scrib* RNAi on the 2nd chromosome (Bloomington/BL38199), UAS-*scrib* RNAi on 3rd
306 chromosome (BL35748), UAS-*dlg* RNAi on the 3rd chromosome (BL35772), y[1] v[1];
307 P{y[+t7.7]=CaryP}attP2 (BL36303, the 3rd chromosome TRiP line background strain),
308 y[1] v[1]; P{y[+t7.7]=CaryP}attP40 (BL36304, the 2nd chromosome TRiP line
309 background strain), engrailed-Gal4 UAS-GFP (BL25752), engrailed-Gal4 (BL30564),
310 UAS-p35 (Hay et al., 1994)(BL6298), Fly-FUCCI (BL55098), worGal4, UAS-
311 cherry::Jupiter, Sqh::GFP (Cabernard and Doe, 2013), c885a-Gal4 (Hrdlicka et al.,
312 2002)(BL6990), UAS-Ras^{V12} (Karim and Rubin, 1998), UAS-Yki^{S168A} (Oh and Irvine,
313 2009)(BL28818), UAS-NICD (Rebay et al., 1993), UAS-Bsk^{DN}(Igaki et al., 2006)(a kind
314 gift from Jose C Pastor-Pareja) , UAS-Tak1^{DN} (BL58811).

315

316 **Immunohistochemistry**

317

318 Around 50 embryos collected within 3 hours were put in an individual vial of fly food to
319 avoid crowding and the larvae were raised at 25-degree incubator for appropriate lengths
320 of time before dissection. Imaginal discs were fixed and stained according to standard
321 protocols. The primary antibodies used were mouse anti-phospho-Histone3 (1:1000, Cell
322 Signaling), rabbit anti-Dcp-1(1:50, Cell Signaling), rabbit anti-phospho-*drosophila* S6
323 (Romero-Pozuelo et al., 2017), goat anti-GFP (1:1000, Abcam) and rabbit anti-DsRed
324 (1:500, Takara). The secondary antibodies conjugated with various Alexa Fluor dyes
325 (ThermoFisher) were used at 1:500. Phalloidin conjugated with Alexa Fluor dyes
326 (1:1000, ThermoFisher) and Hoechst (1:10000, ThermoFisher) were used to stain F-actin
327 and DNA, respectively. For EdU incorporation assay, we labeled the dissected imaginal
328 discs for 30 min before fixation using the Click-iTTM Plus EdU Alexa FluorTM594 Imaging
329 Kit (ThermoFisher). All images were acquired on a Leica TCS SP8 confocal microscope.

330

331 **Western blotting**

332

333 About 30 larvae were dissected in PBS. Cell lysates were homogenized in 1X RIPA
334 (Millipore) with protease inhibitors (Roche). The primary antibodies used were mouse
335 anti-MMP1 (1:100, DSHB) and mouse anti-alpha-tubulin (1:5000, DSHB).

336

337 **Image processing and data analysis**

338

339 Images were taken as z-stacks with a step size of 1 μ m. Tissue volume was measured
340 with Measure Stack plugin in Fiji. PH3+ cell number was calculated with Cell Counter
341 plugin in Fiji. EdU intensity was measured in unit areas from the posterior and anterior
342 region respectively.

343

344 **Fluorescence-activated cell-sorting (FACS) analysis**

345

346 Wing discs were dissected from staged larvae and dissociated for FACS analysis
347 according to standard protocol (Neufeld et al., 1998). Cells were sorted with
348 BDFACS Aria IIIu and data were analyzed with FlowJo.

349

350 ***Drosophila* neuroblast live imaging**

351

352 Female virgins of *hsFLP; worGal4,Sqh::GFP,UASCherry::jupiter; FRT82B/TM6B* were
353 crossed with males of *scribFRT82B/TM6B*. Progeny were heat shocked at 38 degree (in
354 the water bath) for 1 hour and subsequently raised at 25 degree until imaging. Five-day
355 AEL larvae were then dissected and imaged according to standard protocol (Cabernard
356 and Doe, 2013). For wild type control, larvae expressing *wt;*
357 *worGal4,Sqh::GFP,UASCherry::jupiter; Dr/TM6B* were dissected and imaged with the
358 same laser setting as that of the *scrib* mutant neuroblasts.

359

360 **Bulk RNA-seq and data analysis**

361

362 Total RNA was extracted from control and *scrib¹* wing imaginal discs with RNeasy Mini
363 Kit (Qiagen). Construction of cDNA libraries and 150bp paired-end sequencing on

364 Illumina HiSeq platform were performed by Novogene. Cleaned raw reads were mapped
365 to the reference genome using STAR and counts are generated by featuresCounts
366 available in Subread package. PCA analysis was performed in DESeq2. Count
367 normalization was performed using edgeR before hierarchical clustering (hclust function
368 in R).

369

370 **10x Genomics single cell RNA-seq and data analysis**

371

372 Staged *scrib*¹ wing imaginal discs were dissected and transferred to DPBS
373 (ThermoFisher). The wing imaginal discs were dissociated in 0.25% Trypsin-EDTA
374 solution at 37 °C for 10 min. Cells were then washed in DPBS and passed through 35µm
375 filter before library preparation. Construction of 10x single cell libraries and sequencing
376 on Illumina HiSeq platform were performed by Novogene. Raw data mapping and
377 primary analysis was performed in the Cell Ranger pipeline. Secondary analysis for
378 marker gene expression pattern was performed with Cell Ranger R kit and Seurat. Cell
379 type clustering and construction of single-cell pseudotime trajectory using semi-
380 supervised DDRTree method was performed with Monocle (Trapnell et al., 2014).
381 Unstructured and unsupervised topological data analysis (TDA) method was performed
382 for ordering cells (Rizvi et al., 2017). To balance the cell number among stages, we
383 randomly selected 500 cells per stage for each experiment and repeated the experiment
384 for three times. Figures from different repeats were shown in Supplementary Figure 8.

385

386 **Author contributions:**

387

388 Y.Y., T.T.J. and L.Z. designed the experiments. T.T.J., L.Z. and Y.W. performed all the
389 experiments except Figure S3. Y.Y., M.X.D. and T.T.J. analyzed all the data and
390 prepared all the figures except Figure S3. S.S.H. and J.G.W provided RNA sequencing
391 data analysis tools, performed TDA, prepared Figure 4F, Figure S6 and Figure S8. P.T.,
392 A.A.S, V.S and C.C. performed experiments for Figure S3 and prepared Figure S3. Y.Y.
393 wrote the manuscript with input from J.G.W. and C.C.

394

395 **Acknowledgements**

396 We thank Dr. Chris Doe and Dr. Jose C Pastor-Pareja, Bloomington Stock Center and
397 Developmental Biology Hybridoma Bank for providing fly stocks and reagents. We
398 thank Dr. Zilong Wen and Dr. Mingjie Zhang for sharing their confocal microscope. We
399 thank Dr. Chris Doe and Dr. Trudi Schupbach for helpful comments on the manuscript.
400 We thank Dr. Tatsushi Igaki for helpful discussion on the project. This work was
401 supported by grants to Yan Yan from the Research Grants Council of the Hong Kong
402 Special Administrative Region (grants GRF16103314, 16103815, 16150016, AoE/M-
403 09/12) and to Jiguang Wang from from a NSFC/RGC Grant No. N_HKUST601/17 and a
404 CRF Grant No. C6002-17G.

405

406 **References:**

407 Bilder, D. (2004). Epithelial polarity and proliferation control: links from the
408 *Drosophila* neoplastic tumor suppressors. *Genes Dev* 18, 1909-1925.
409 Bilder, D., Li, M., and Perrimon, N. (2000). Cooperative regulation of cell polarity and
410 growth by *Drosophila* tumor suppressors. *Science* 289, 113-116.
411 Bilder, D., and Perrimon, N. (2000). Localization of apical epithelial determinants by
412 the basolateral PDZ protein Scribble. *Nature* 403, 676-680.
413 Boggiano, J.C., and Fehon, R.G. (2012). Growth control by committee: intercellular
414 junctions, cell polarity, and the cytoskeleton regulate Hippo signaling. *Dev Cell* 22,
415 695-702.
416 Brumby, A.M., and Richardson, H.E. (2003). scribble mutants cooperate with
417 oncogenic Ras or Notch to cause neoplastic overgrowth in *Drosophila*. *EMBO J* 22,
418 5769-5779.
419 Bunker, B.D., Nellimoottil, T.T., Boileau, R.M., Classen, A.K., and Bilder, D. (2015). The
420 transcriptional response to tumorigenic polarity loss in *Drosophila*. *Elife* 4.
421 Cabernard, C., and Doe, C.Q. (2013). Live imaging of neuroblast lineages within
422 intact larval brains in *Drosophila*. *Cold Spring Harb Protoc* 2013, 970-977.
423 Chen, C.L., Schroeder, M.C., Kango-Singh, M., Tao, C., and Halder, G. (2012). Tumor
424 suppression by cell competition through regulation of the Hippo pathway. *Proc Natl*
425 *Acad Sci U S A* 109, 484-489.
426 Cordero, J.B., Macagno, J.P., Stefanatos, R.K., Strathdee, K.E., Cagan, R.L., and Vidal, M.
427 (2010). Oncogenic Ras diverts a host TNF tumor suppressor activity into tumor
428 promoter. *Dev Cell* 18, 999-1011.
429 Figueroa-Clavevega, A., and Bilder, D. (2015). Malignant *Drosophila* tumors
430 interrupt insulin signaling to induce cachexia-like wasting. *Dev Cell* 33, 47-55.
431 Gateff, E. (1978). Malignant neoplasms of genetic origin in *Drosophila melanogaster*.
432 *Science* 200, 1448-1459.
433 Gonzalez, C. (2013). *Drosophila melanogaster*: a model and a tool to investigate
434 malignancy and identify new therapeutics. *Nat Rev Cancer* 13, 172-183.

435 Hanahan, D., and Weinberg, R.A. (2000). The hallmarks of cancer. *Cell* *100*, 57-70.
436 Hay, B.A., Wolff, T., and Rubin, G.M. (1994). Expression of baculovirus P35 prevents
437 cell death in *Drosophila*. *Development* *120*, 2121-2129.
438 Hrdlicka, L., Gibson, M., Kiger, A., Micchelli, C., Schober, M., Schock, F., and Perrimon,
439 N. (2002). Analysis of twenty-four Gal4 lines in *Drosophila melanogaster*. *Genesis*
440 *34*, 51-57.
441 Igaki, T., Pagliarini, R.A., and Xu, T. (2006). Loss of cell polarity drives tumor growth
442 and invasion through JNK activation in *Drosophila*. *Curr Biol* *16*, 1139-1146.
443 Johnston, L.A. (2009). Competitive interactions between cells: death, growth, and
444 geography. *Science* *324*, 1679-1682.
445 Karim, F.D., and Rubin, G.M. (1998). Ectopic expression of activated Ras1 induces
446 hyperplastic growth and increased cell death in *Drosophila* imaginal tissues.
447 *Development* *125*, 1-9.
448 Katheder, N.S., Khezri, R., O'Farrell, F., Schultz, S.W., Jain, A., Rahman, M.M., Schink,
449 K.O., Theodossiou, T.A., Johansen, T., Juhasz, G., *et al.* (2017). Microenvironmental
450 autophagy promotes tumour growth. *Nature* *541*, 417-420.
451 McGranahan, N., and Swanton, C. (2017). Clonal Heterogeneity and Tumor
452 Evolution: Past, Present, and the Future. *Cell* *168*, 613-628.
453 Morais da Silva, S., Moutinho-Santos, T., and Sunkel, C.E. (2013). A tumor suppressor
454 role of the Bub3 spindle checkpoint protein after apoptosis inhibition. *J Cell Biol* *201*,
455 385-393.
456 Morata, G., and Ripoll, P. (1975). Minutes: mutants of *drosophila* autonomously
457 affecting cell division rate. *Dev Biol* *42*, 211-221.
458 Neufeld, T.P., de la Cruz, A.F., Johnston, L.A., and Edgar, B.A. (1998). Coordination of
459 growth and cell division in the *Drosophila* wing. *Cell* *93*, 1183-1193.
460 Nordling, C.O. (1953). A new theory on cancer-inducing mechanism. *Br J Cancer* *7*,
461 68-72.
462 Oh, H., and Irvine, K.D. (2009). In vivo analysis of Yorkie phosphorylation sites.
463 *Oncogene* *28*, 1916-1927.
464 Pagliarini, R.A., and Xu, T. (2003). A genetic screen in *Drosophila* for metastatic
465 behavior. *Science* *302*, 1227-1231.
466 Pastor-Pareja, J.C., and Xu, T. (2013). Dissecting social cell biology and tumors using
467 *Drosophila* genetics. *Annu Rev Genet* *47*, 51-74.
468 Rebay, I., Fehon, R.G., and Artavanis-Tsakonas, S. (1993). Specific truncations of
469 *Drosophila* Notch define dominant activated and dominant negative forms of the
470 receptor. *Cell* *74*, 319-329.
471 Richardson, H.E., and Portela, M. (2018). Modelling Cooperative Tumorigenesis in
472 *Drosophila*. *Biomed Res Int* *2018*, 4258387.
473 Rizvi, A.H., Camara, P.G., Kandror, E.K., Roberts, T.J., Schieren, I., Maniatis, T., and
474 Rabadan, R. (2017). Single-cell topological RNA-seq analysis reveals insights into
475 cellular differentiation and development. *Nat Biotechnol* *35*, 551-560.
476 Romero-Pozuelo, J., Demetriades, C., Schroeder, P., and Teleman, A.A. (2017).
477 CycD/Cdk4 and Discontinuities in Dpp Signaling Activate TORC1 in the *Drosophila*
478 Wing Disc. *Dev Cell* *42*, 376-387 e375.
479 Simpson, P. (1979). Parameters of cell competition in the compartments of the wing
480 disc of *Drosophila*. *Dev Biol* *69*, 182-193.

481 Simpson, P., and Morata, G. (1981). Differential mitotic rates and patterns of growth
482 in compartments in the *Drosophila* wing. *Dev Biol* 85, 299-308.
483 Sonoshita, M., and Cagan, R.L. (2017). Modeling Human Cancers in *Drosophila*. *Curr*
484 *Top Dev Biol* 121, 287-309.
485 Sun, S., and Irvine, K.D. (2016). Cellular Organization and Cytoskeletal Regulation of
486 the Hippo Signaling Network. *Trends Cell Biol* 26, 694-704.
487 Trapnell, C., Cacchiarelli, D., Grimsby, J., Pokharel, P., Li, S., Morse, M., Lennon, N.J.,
488 Livak, K.J., Mikkelsen, T.S., and Rinn, J.L. (2014). The dynamics and regulators of cell
489 fate decisions are revealed by pseudotemporal ordering of single cells. *Nat*
490 *Biotechnol* 32, 381-386.
491 Vaughn, J., and Igaki, T. (2016). Slit-Robo Repulsive Signaling Extrudes
492 Tumorigenic Cells from Epithelia. *Dev Cell* 39, 683-695.
493 Woods, D.F., and Bryant, P.J. (1991). The discs-large tumor suppressor gene of
494 *Drosophila* encodes a guanylate kinase homolog localized at septate junctions. *Cell*
495 66, 451-464.
496 Yamamoto, M., Ohsawa, S., Kunimasa, K., and Igaki, T. (2017). The ligand Sas and its
497 receptor PTP10D drive tumour-suppressive cell competition. *Nature* 542, 246-250.
498 Zeidler, M.P., Perrimon, N., and Strutt, D.I. (1999). Polarity determination in the
499 *Drosophila* eye: a novel role for unpaired and JAK/STAT signaling. *Genes Dev* 13,
500 1342-1353.
501 Zielke, N., Korzelius, J., van Straaten, M., Bender, K., Schuhknecht, G.F., Dutta, D.,
502 Xiang, J., and Edgar, B.A. (2014). Fly-FUCCI: A versatile tool for studying cell
503 proliferation in complex tissues. *Cell Rep* 7, 588-598.
504

505 **Figure legends**

506

507 **Figure 1 The Scrib-depleted cells display different growth rates over time.**

508

509 (A) Examples of a control 5-day AEL imaginal disc and *scrib*¹ mutant wing imaginal
510 discs from 4-day AEL to 10-day AEL stained for actin (red) and DNA (blue). Control
511 genotype: *FRT82B*. Scale bar: 10 μ m.

512

513 (B) Quantification of volumes for control and *scrib*¹ mutant wing imaginal discs over
514 time. Control genotype: *FRT82B* raised at identical conditions. Control, **4d** n = 10,
515 $5\pm 1\times 10^5\mu\text{m}^3$, **5d** n = 19, $1.9\pm 0.4\times 10^6\mu\text{m}^3$; *scrib*¹ mutant, **4d** n = 16, $1.4\pm 0.3\times 10^5\mu\text{m}^3$, **5d** n
516 = 18, $5\pm 2\times 10^5\mu\text{m}^3$, **6d** n = 19, $7\pm 2\times 10^5\mu\text{m}^3$, **7d** n = 17, $2.0\pm 0.7\times 10^6\mu\text{m}^3$, **8d** n = 14,
517 $3\pm 1\times 10^6\mu\text{m}^3$, **9d** n = 17, $4\pm 1\times 10^6\mu\text{m}^3$, **10d** n = 11, $6\pm 2\times 10^6\mu\text{m}^3$. Note that larvae from
518 the control group become pupae at 5-day AEL.

519

520 (C-F) 4-day AEL (C-D) and 5-day AEL (E-F) control (C and E) and *scrib*¹ mutant (D and
521 F) wing imaginal discs stained for PH3(green), actin (red) and DNA (blue). Control
522 genotype: *FRT82B*. Scale bar: 10 μ m.

523

524 (G) Quantification of PH3⁺ cell number per unit volume ($10^5\mu\text{m}^3$) in 4-day AEL and 5-
525 day AEL control and *scrib*¹ mutant wing imaginal discs. Statistical analysis was
526 performed by unpaired t-test. Control, *FRT82B*, **4d** n = 10, 37 ± 5 , **5d** n = 19, 26 ± 3 ; *scrib*¹
527 mutant, **4d** n = 16, 22 ± 4 , **5d** n = 18, 25 ± 3 .

528

529 (H-U) 4-day (H-J), 5-day (M-O) and 6-day (R-S) AEL *scribRNAi* (H, M, R), *dlgRNAi* (I,
530 N, S) and control (J, O) imaginal discs stained for PH3 (gray), actin(red) and GFP
531 (green). Quantification of volumes (K, P, T) and PH3⁺ cell number per unit volume
532 ($10^5\mu\text{m}^3$) (L, Q, U) for 4-day (K, L), 5-day (P, Q) and 6-day (T, U) AEL *scribRNAi*,
533 *dlgRNAi* and control imaginal discs. Genotype for the *scribRNAi* group: *engrailed-Gal4*
534 *UAS-GFP/+; UAS-scribRNAi/+*. Genotype for the *dlgRNAi* group: *engrailed-Gal4 UAS-*
535 *GFP/+; UAS-dlgRNAi/+*. Genotype for the control group: *engrailed-Gal4 UAS-GFP/+;*

536 *P{y[+t7.7]=CaryP}attP2* /+ (the 3rd chromosome TRiP line background strain). The
537 *scribRNAi* group, **4d** n = 15, anterior, $2.6 \pm 0.5 \times 10^5 \mu\text{m}^3$, PH+ cell number 37 ± 5 , posterior,
538 $4 \pm 1 \times 10^4 \mu\text{m}^3$, PH+ cell number 14 ± 8 , **5d** n = 14, anterior, $4.3 \pm 0.9 \times 10^5 \mu\text{m}^3$, PH+ cell
539 number 29 ± 5 , posterior, $8 \pm 4 \times 10^4 \mu\text{m}^3$, PH+ cell number 21 ± 6 , **6d** n = 15, anterior,
540 $8 \pm 2 \times 10^5 \mu\text{m}^3$, PH+ cell number 13 ± 3 , posterior, $3 \pm 2 \times 10^5 \mu\text{m}^3$, PH+ cell number 25 ± 4 ; The
541 *dlgRNAi* group, **4d** n = 16, anterior, $3.0 \pm 0.5 \times 10^5 \mu\text{m}^3$, PH+ cell number 34 ± 9 , posterior,
542 $5 \pm 2 \times 10^4 \mu\text{m}^3$, PH+ cell number 11 ± 8 , **5d** n = 17, anterior, $8 \pm 2 \times 10^5 \mu\text{m}^3$, PH+ cell number
543 16 ± 5 , posterior, $3 \pm 1 \times 10^5 \mu\text{m}^3$, PH+ cell number 25 ± 9 , **6d** n = 16, anterior, $9 \pm 2 \times 10^5 \mu\text{m}^3$,
544 PH+ cell number 16 ± 5 , posterior, $4 \pm 2 \times 10^5 \mu\text{m}^3$, PH+ cell number 33 ± 7 ; The control
545 group, **4d** n = 16, anterior, $2.5 \pm 0.6 \times 10^5 \mu\text{m}^3$, PH+ cell number 44 ± 8 , posterior,
546 $1.3 \pm 0.3 \times 10^5 \mu\text{m}^3$, PH+ cell number 43 ± 6 , **5d** n = 13, anterior, $6 \pm 1 \times 10^5 \mu\text{m}^3$, PH+ cell
547 number 25 ± 4 , posterior, $4 \pm 1 \times 10^5 \mu\text{m}^3$, PH+ cell number 28 ± 4 . Scale bar: $10 \mu\text{m}$.
548 Statistical analysis was performed by unpaired t-test. Note that larvae from the control
549 group become pupae at 5-day AEL.

550

551 **Figure 2 The Scrib-depleted cells display different cell cycle profiles over time.**

552

553 (A-E) 4-day AEL (A-B) and 5-day AEL (C-D) control (A and C) and *scribRNAi* (B and
554 D) wing imaginal discs stained for EdU (red in A, B, C, D and gray in A', B', C', D'),
555 GFP (green) and DNA (blue). (E) Quantification of posterior/anterior EdU intensity ratio
556 for 4-day and 5-day AEL control and *scribRNAi* wing imaginal discs. Genotype for the
557 *scribRNAi* group: *engrailed-Gal4 UAS-GFP/+; UAS-scribRNAi/+*. Genotype for the
558 control group: *engrailed-Gal4 UAS-GFP/+; P{y[+t7.7]=CaryP}attP2 /+*. The *scribRNAi*
559 group, 4d n = 8, 5d n = 10; The control group, 4d n = 9, 5d n = 10. Statistical analysis
560 was performed by unpaired t-test. Scale bar: $10 \mu\text{m}$.

561

562 (F-H) FACS analysis of DNA contents of control and *scribRNAi* cells from 4-day (F), 5-
563 day (G) and 6-day (H) AEL wing imaginal discs. Genotype for FACS analysis: *engrailed-*
564 *Gal4 UAS-GFP/+; UAS-scribRNAi/+*. The anterior GFP- cells serve as control and the
565 posterior GFP+ cells are the *scribRNAi* cells. Because the number of GFP- cells is much
566 larger than GFP+ cells, the histogram overlay is normalized using the unit distribution

567 mode in FlowJo. At least five thousand cells were recorded for each cell group. Each
568 experiment is replicated for at least three times.

569

570 (I-J) FACS analysis of DNA contents of control and *scrib*¹ mutant cells from 4-day (I)
571 and 5-day (J) AEL wing imaginal discs. Genotype for the control group: *FRT82B* raised
572 at identical conditions. At least five thousand cells were recorded for each cell group.
573 Each experiment is replicated for at least three times.

574

575 **Figure 3 High JNK signaling activity causes growth arrest in early *scrib* mutant**
576 **tumors.**

577

578 (A) Principle component analysis (PCA) of transcriptomes from 5-day AEL control
579 imaginal discs and 5-day, 6-day, 8-day and 10-day AEL *scrib* mutant wing imaginal
580 discs. Control genotype: *FRT82B*. Four biological replicates are plotted for each time
581 point except for 6-day AEL groups which only three biological replicates are recovered.

582

583 (B) Hierarchical clustering of transcriptomes from 5-day, 6-day, 8-day and 10-day AEL
584 *scrib* mutant wing imaginal discs.

585

586 (C) Plot of JNK signaling reporter genes in staged *scrib* mutant wing discs normalized by
587 those in 5-day AEL control imaginal discs using log₂(FPKM fold change) values. Control
588 genotype: *FRT82B*.

589

590 (D) Western blot analysis of Mmp-1 protein level in 5-day AEL control imaginal discs,
591 5-day and 8-day AEL *scrib* mutant wing imaginal discs. Control genotype: *FRT82B*.

592

593 (E-J) 4-day (E-G) and 5-day (H-J) AEL *bsk*^{DN} (E, H), *scribRNAi* (F, I) and *scribRNAi*
594 *bsk*^{DN} (G, J) imaginal discs stained for actin (red) and GFP (green). Genotype for (E) and
595 (H): *engrailed-Gal4 UAS-GFP/+; UAS- bsk*^{DN}/+. Genotype for (F) and (I): *engrailed-*
596 *Gal4 UAS-GFP/UAS-scribRNAi*. Genotype of (G) and (J): *engrailed-Gal4 UAS-*
597 *GFP/UAS-scribRNAi; UAS- bsk*^{DN}/+. Scale bar: 10µm.

598

599 (K-L) Quantification of volumes for 4-day (K) and 5-day (L) AEL *bsk^{DN}*, *scribRNAi* and
600 *scribRNAi bsk^{DN}* imaginal discs. *bsk^{DN}*, **4d** n = 17, anterior, $1.7 \pm 0.7 \times 10^5 \mu\text{m}^3$, posterior,
601 $8 \pm 4 \times 10^4 \mu\text{m}^3$, **5d** n = 17, anterior, $5 \pm 2 \times 10^5 \mu\text{m}^3$, posterior, $4 \pm 1 \times 10^5 \mu\text{m}^3$. *scribRNAi*, **4d** n =
602 20, anterior, $2.0 \pm 0.5 \times 10^5 \mu\text{m}^3$, posterior, $4 \pm 1 \times 10^4 \mu\text{m}^3$, **5d** n = 15, anterior, $4 \pm 1 \times 10^5 \mu\text{m}^3$,
603 posterior, $8 \pm 4 \times 10^4 \mu\text{m}^3$. *scribRNAi bsk^{DN}*, **4d** n = 14, anterior, $1.4 \pm 0.4 \times 10^5 \mu\text{m}^3$, posterior,
604 $6 \pm 2 \times 10^4 \mu\text{m}^3$, **5d** n = 8, anterior, $4.2 \pm 0.5 \times 10^5 \mu\text{m}^3$, posterior, $2.4 \pm 0.8 \times 10^5 \mu\text{m}^3$. Statistical
605 analysis was performed by unpaired t-test.

606

607 (M-R) 4-day AEL control (M), *scribRNAi* (N), *scribRNAi Tak1^{DN}*(O), *scribRNAi*
608 *Yki^{S168A}*(P), *scribRNAi Ras^{V12}*(Q), and *scribRNAi NICD* (R) imaginal discs stained for
609 actin (red). Genotypes are as follows: (M) *C885a-Gal4/+; UAS-GFP/+*; (N) *C885a-*
610 *Gal4/+; UAS-scribRNAi /+*; (O) *C885a-Gal4/UAS-Tak1^{DN}; UAS-scribRNAi/+*; (P)
611 *C885a-Gal4/UAS-Yki^{S168A}; UAS-scribRNAi/+*; (Q) *C885a-Gal4/UAS-Ras^{V12}; UAS-*
612 *scribRNAi/+*; (R) *C885a-Gal4/UAS-NICD; UAS-scribRNAi/+*. Scale bar: 10 μm .

613

614 (S) Barplot of volumes for 4-day AEL control (n = 33, $1.0 \pm 0.3 \times 10^6 \mu\text{m}^3$), *scribRNAi* (n =
615 30, $5 \pm 1 \times 10^5 \mu\text{m}^3$), *scribRNAi Tak1^{DN}* (n = 35, $1.1 \pm 0.2 \times 10^6 \mu\text{m}^3$), *scribRNAi Yki^{S168A}* (n =
616 26, $7 \pm 2 \times 10^5 \mu\text{m}^3$), *scribRNAi Ras^{V12}* (n = 30, $4 \pm 2 \times 10^5 \mu\text{m}^3$), and *scribRNAi NICD* (n =
617 18, $2.1 \pm 0.4 \times 10^5 \mu\text{m}^3$) imaginal discs.

618

619 (T) Quantification of volumes for control, *scribRNAi*, *scribRNAi Tak1^{DN}*, *scribRNAi*
620 *Yki^{S168A}*, *scribRNAi Ras^{V12}*, and *scribRNAi NICD* imaginal discs over time. Control, **4d** n
621 = 33, $1.0 \pm 0.3 \times 10^6 \mu\text{m}^3$; **5d** n = 26, $2.1 \pm 0.6 \times 10^6 \mu\text{m}^3$. *scribRNAi*, **4d** n = 30, $5 \pm 1 \times 10^5 \mu\text{m}^3$;
622 **5d** n = 27, $1.4 \pm 0.5 \times 10^6 \mu\text{m}^3$; **6d** n = 34, $3 \pm 1 \times 10^6 \mu\text{m}^3$; **7d** n = 34, $6 \pm 2 \times 10^6 \mu\text{m}^3$; **8d** n = 32,
623 $8 \pm 3 \times 10^6 \mu\text{m}^3$. *scribRNAi Tak1^{DN}*, **4d** n = 35, $1.1 \pm 0.2 \times 10^6 \mu\text{m}^3$; **5d** n = 39, $3 \pm 1 \times 10^6 \mu\text{m}^3$; **6d**
624 n = 32, $6 \pm 3 \times 10^6 \mu\text{m}^3$. *scribRNAi Yki^{S168A}*, **4d** n = 26, $7 \pm 2 \times 10^5 \mu\text{m}^3$; **5d** n = 30,
625 $1.9 \pm 0.8 \times 10^6 \mu\text{m}^3$; **6d** n = 32, $5 \pm 1 \times 10^6 \mu\text{m}^3$; **7d** n = 28, $9 \pm 3 \times 10^6 \mu\text{m}^3$; **8d** n = 34,
626 $1.1 \pm 0.4 \times 10^7 \mu\text{m}^3$. *scribRNAi Ras^{V12}*, **4d** n = 30, $4 \pm 2 \times 10^5 \mu\text{m}^3$; **5d** n = 35, $1.9 \pm 0.4 \times 10^6 \mu\text{m}^3$;
627 **6d** n = 30, $7 \pm 2 \times 10^6 \mu\text{m}^3$; **7d** n = 28, $1.1 \pm 0.4 \times 10^7 \mu\text{m}^3$; **8d** n = 28, $1.6 \pm 0.6 \times 10^7 \mu\text{m}^3$.

628 *scribRNAi NICD*, **4d** n = 18, $2.1 \pm 0.4 \times 10^5 \mu\text{m}^3$; **5d** n = 20, $3 \pm 2 \times 10^5 \mu\text{m}^3$; **6d** n = 21,
629 $5 \pm 3 \times 10^5 \mu\text{m}^3$; **7d** n = 18, $2.5 \pm 0.7 \times 10^5 \mu\text{m}^3$; **8d** n = 25, $2.2 \pm 0.4 \times 10^5 \mu\text{m}^3$.

630

631 **Figure 4 Visualization of single cells from the *scrib* mutant tumors in the reduced**
632 **dimensional space.**

633

634 (A-B) Visualization of single cells ordered in the t-SNE reduced dimensional space
635 colored by cell types defined by *Mmp1* and *kek1* expression level (A) (normalized
636 expression level=1 as threshold), and tumor age (B). Single cells pooled from 4-day, 5-
637 day and 8-day AEL *scrib* mutant tumors. 3000 single cells per time point are randomly
638 sampled.

639

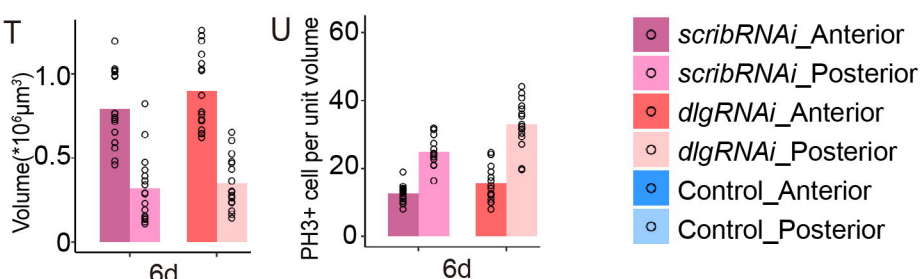
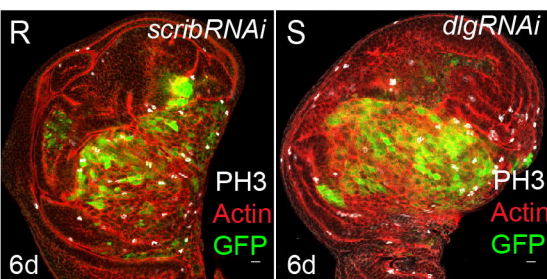
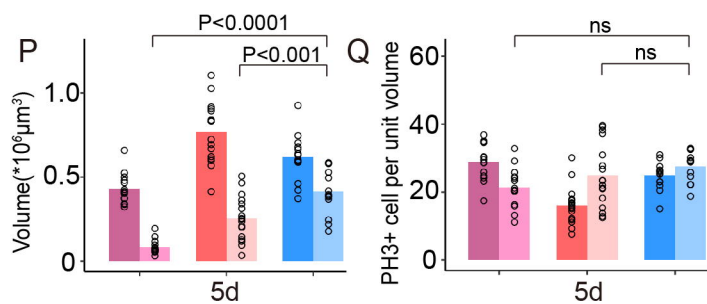
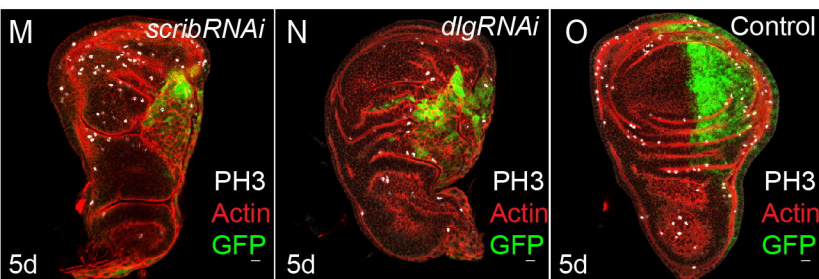
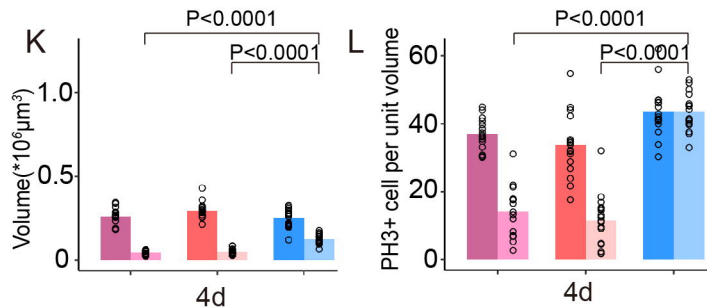
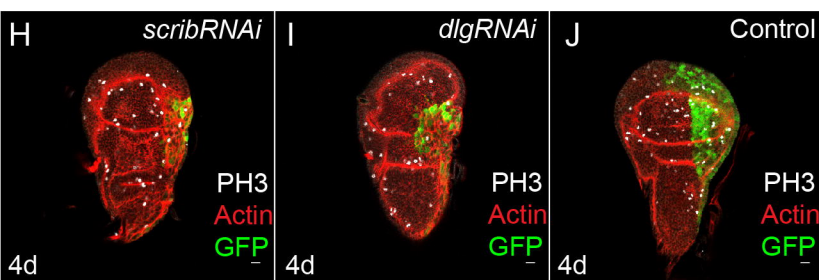
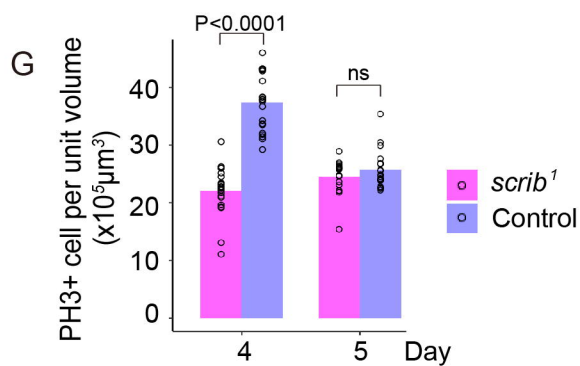
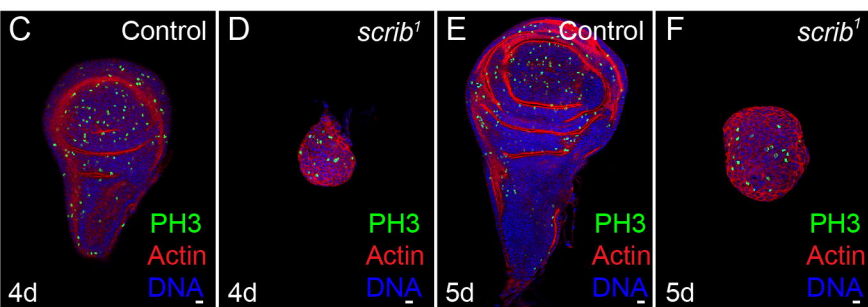
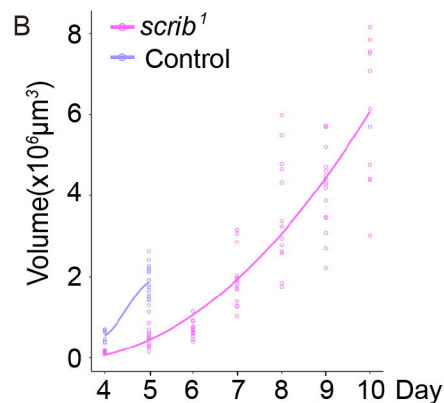
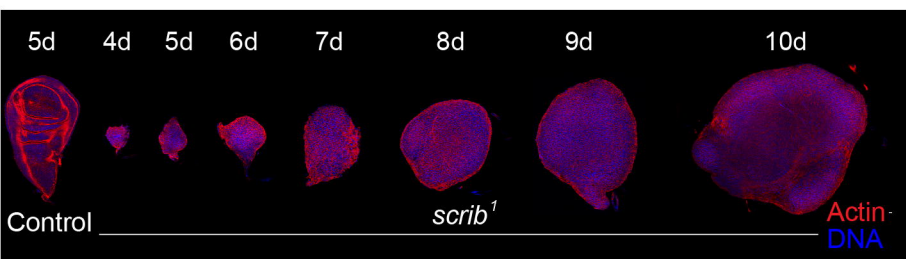
640 (C-E) Visualization of single cells ordered along a pseudotime trajectory in the reduced
641 dimensional space colored by pseudotime (C), cell types defined by *Mmp1* and *kek1*
642 expression level (D) (normalized expression level=1 as threshold), and tumor age (E).
643 3000 single cells per time point are randomly sampled.

644

645 (F) Topological representation of single cells ordered using scTDA. 500 cells per time
646 point are randomly sampled. The nodes (circles) are clusters of single cells with similar
647 global expression profiles, and the node size corresponds to the number of cells in that
648 cluster. Edges (lines) connect clusters that have at least one cell in common. The node
649 color in the left panel indicates the time line of the *scrib* mutant tumor progression. A
650 node composed of a mixture of cells from early and late stages has an intermediate color.
651 The node color in the right panel indicates the expression level of marker genes labeled in
652 each panel.

Figure 1

A



○ *scribRNAi*_Anterior
○ *scribRNAi*_Posterior
○ *dlgRNAi*_Anterior
○ *dlgRNAi*_Posterior
○ Control_Anterior
○ Control_Posterior

Figure 2

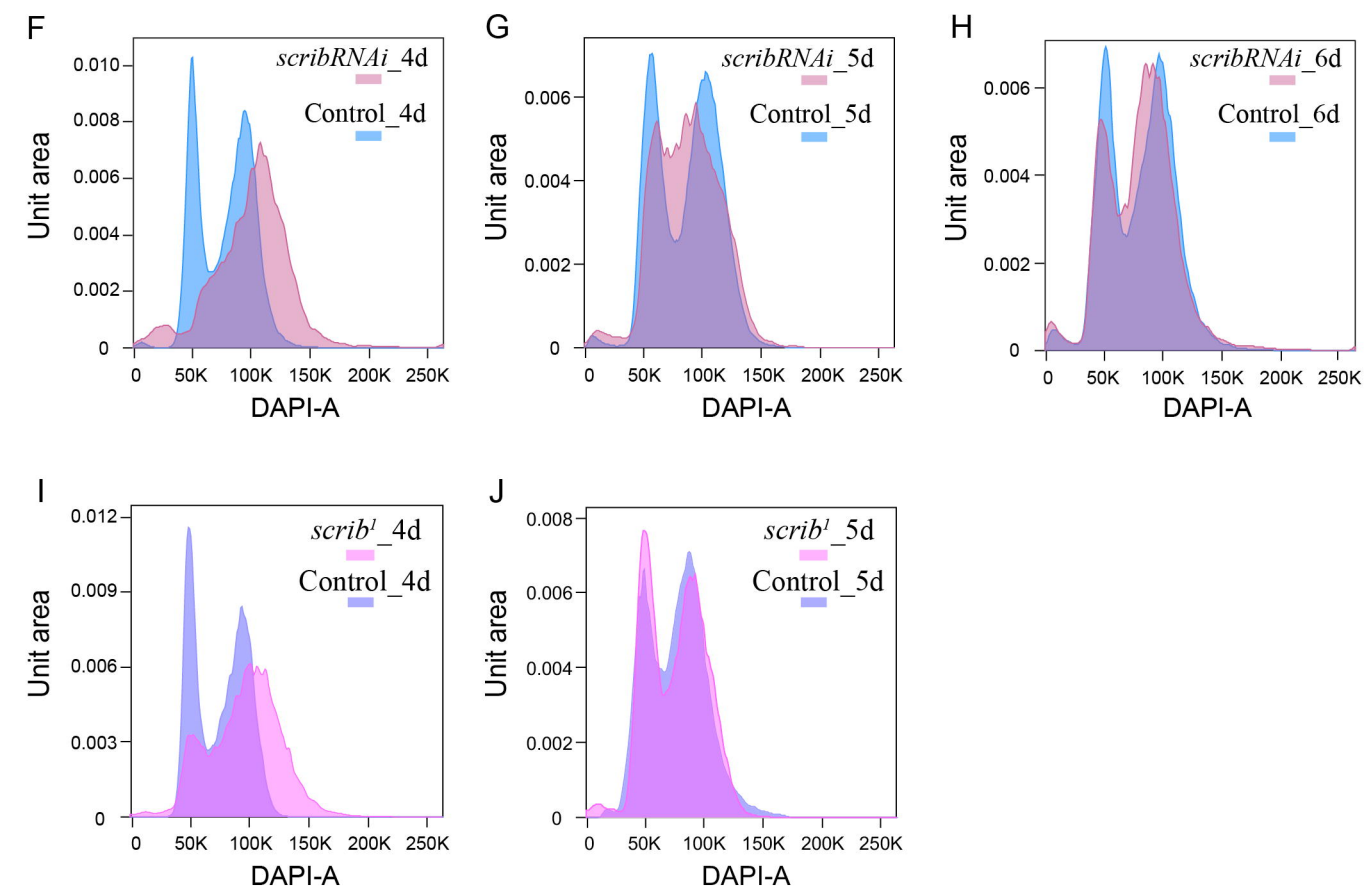
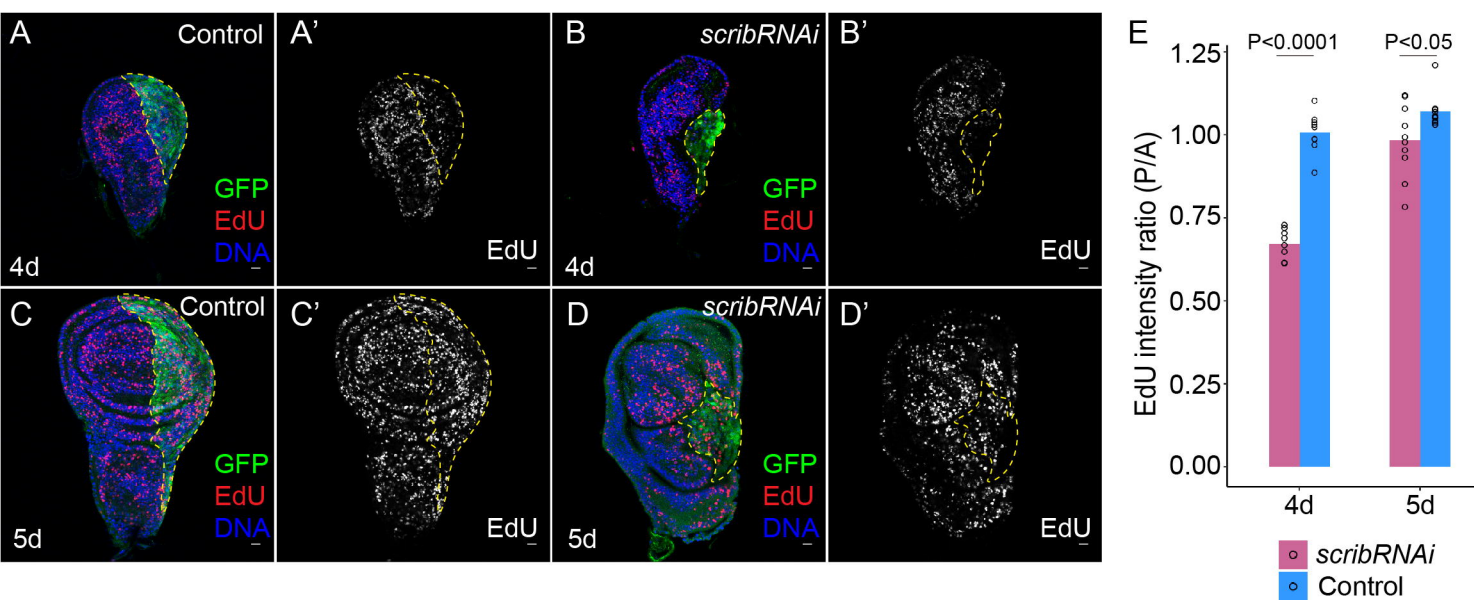


Figure 3

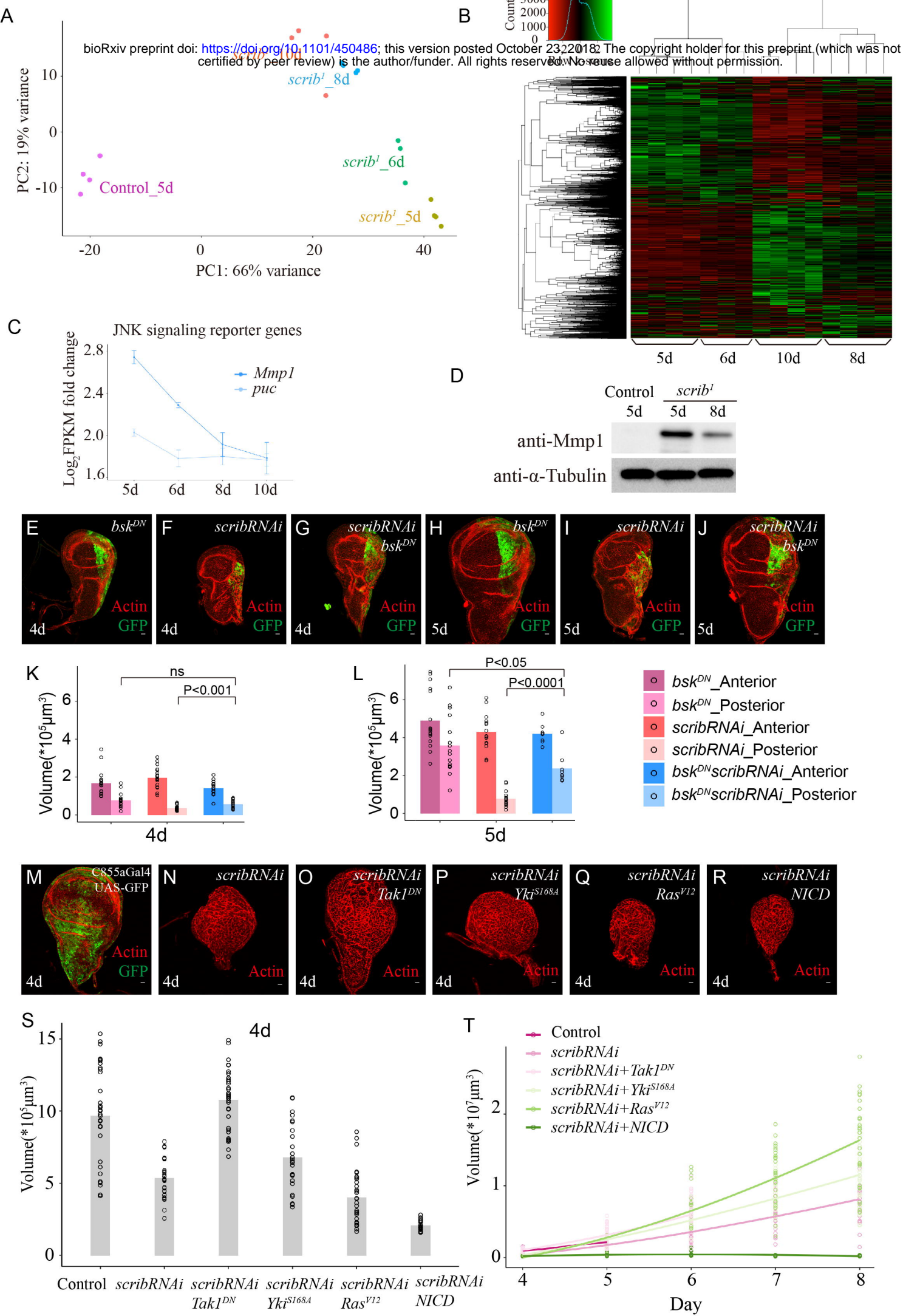


Figure 4

